OPTICA

Microcavity platform for widely tunable optical double resonance

Sigurd Flågan,[1,2] Patrick Maletinsky,[1] Richard J. Warburton,[1] and
Daniel Riedel[1,3,*]

[1]*Department of Physics, University of Basel, Klingelbergstrasse 82, Basel CH-4056, Switzerland*
[2]*Currently at Institute for Quantum Science and Technology, University of Calgary, Calgary, Alberta T2N 1N4, Canada*
[3]*Currently at E. L. Ginzton Laboratory, Stanford University, Stanford, California 94305, USA*
*Corresponding author: riedeld@stanford.edu

Tunable open-access Fabry–Perot microcavities are versatile and widely applied in different areas of photonics research. The open geometry of such cavities enables the flexible integration of thin dielectric membranes. Efficient coupling of solid-state emitters in various material systems has been demonstrated based on the combination of high quality factors and small mode volumes with a large-range *in situ* tunability of the optical resonance frequency. Here, we demonstrate that by incorporating a diamond micromembrane with a small thickness gradient, both the absolute frequency and the frequency difference between two resonator modes can be controlled precisely. Our platform allows both the mirror separation and, by lateral displacement, the diamond thickness to be tuned. These two independent tuning parameters enable the double-resonance enhancement of nonlinear optical processes with the capability of tuning the pump laser over a wide frequency range. As a proof of concept, we demonstrate a > THz continuous tuning range of doubly resonant Raman scattering in diamond, a range limited only by the reflective stopband of the mirrors. Based on the experimentally determined quality factors exceeding 300,000, our theoretical analysis suggests that, with realistic improvements, a ∼mW threshold for establishing Raman lasing is within reach. Our findings pave the way to the creation of a universal, low-power frequency shifter. The concept can be applied to enhance other nonlinear processes such as second harmonic generation or optical parametric oscillation across different material platforms. © 2022 Optica Publishing Group under the terms of the Optica Open Access Publishing Agreement

1. INTRODUCTION

The strong confinement in optical nano- and microresonators can greatly enhance the interaction between light and matter [1,2]. In the context of nonlinear optics, whispering-gallery modes in microdisk, microring, and racetrack resonators stand out since they combine large optical quality (Q) factors with small mode volumes (V) [3–6]. Such monolithic microresonators have been made from a variety of different materials including, but not limited to, diamond [7–10], silica [11,12], silicon carbide [13–15], silicon nitride [16–18], lithium niobate [19,20], gallium phosphide [21–24], and hexagonal boron nitride [25].

Efficient enhancement of nonlinear optical processes in a microcavity requires simultaneous resonant enhancement of all the optical fields involved. The resonance frequencies in monolithic resonators are set by the device geometry [26]. Therefore, careful tailoring of the device cross section [27] or modulation of the device radius [28,29] is required for frequency matching at distinct frequencies. Fabrication imperfections, however, limit the device yield. Hence, typically a large matrix of devices with varying parameters is required to achieve a desired frequency configuration. Certain tuning mechanisms such as gas condensation [13],

thermo-optic effects [21] and strain [30] allow the global dispersion profile to be adjusted. An *in situ* technique to tune the absolute and relative frequencies of certain modes, required for achieving multi-resonant configurations, remains elusive. In principle, crossed-fiber-based tunable optical Fabry–Perot microcavities could be used for this purpose [31,32]. In practice, however, implementing such crossed fiber microcavities comprising a nonlinear optical material constitutes a major technological challenge. Furthermore, small mode volumes for the crossed resonators are prevented by the device geometry.

Nevertheless, the integration of a thin dielectric membrane into an individual highly miniaturized Fabry–Perot cavity represents an appealing approach to enhance nonlinear optical processes. Such "open microcavities" offer a high Q/V ratio [33] and thereby promote strong light–matter interactions [2,34]. In addition, the platform offers full *in situ* tunability of its resonance frequencies upon changing the mirror separation. Importantly, the full mode dispersion of a membrane-in-the-middle cavity depends on both the membrane thickness and the separation of the mirrors [33,35].

Here, we show that the dependence on membrane thickness can be exploited as an additional tuning mechanism. By controlling

both the vertical separation of the two mirrors and the lateral position of the cavity with respect to the membrane, both the absolute frequency and the relative frequency splitting between two distinct modes can be tuned.

We implement such a platform by embedding a diamond micromembrane into an open microcavity, which exhibits a small thickness gradient, i.e., a wedge. As a proof-of-principle experiment, we focus on the doubly resonant enhancement of Raman scattering from the diamond membrane [36]. Raman-scattered light is generated when, upon the creation of a phonon, incoming pump photons are redshifted by the fixed phonon energy. Diamond is particularly suited for testing our platform based on the combination of a large Raman gain ($\sim 75\,\mathrm{GW} \cdot \mathrm{cm}^{-1}$ at 532 nm) [37], a large Raman shift ($\sim 1{,}332\,\mathrm{cm}^{-1}$, $\sim 40\,\mathrm{THz}$) [38] and a narrow gain linewidth ($\Delta \nu_R \sim 40\,\mathrm{GHz}$) [39–41].

By tuning the mirror separation, we show that we are able to establish a double-resonance condition, where the frequency separation between two fundamental modes ν_1 and ν_2 corresponds exactly to the Raman shift, i.e., $\nu_1 - \nu_2 = \Delta\nu_R$. Hence, via precise tuning of the pump frequency to ν_1, the pump laser and the Raman transition are each brought into resonance with a cavity mode simultaneously leading to a strong enhancement of the creation of Stokes photons at frequency ν_2. Importantly, for our device, this double-resonance condition is not limited to one pair of frequencies, but it can be continuously tuned *in situ* over a >THz range by exploiting the thickness gradient of the diamond membrane. Experimentally, this is achieved simply by first displacing the diamond membrane laterally with respect to the cavity mode and then adjusting the mirror separation accordingly. In our implementation, the tuning range is limited by the overall change in thickness of the membrane, but in principle, a double-resonance condition with fixed frequency difference can be established across the whole reflective stopband of the mirrors corresponding to several tens of THz.

2. METHODS

Our plano–concave microcavity design supports Gaussian fundamental modes [Fig. 1(a)] [35,42–46]. The microcavity is formed by two mirror-coated fused silica substrates, one of which contains an array of spherical micromirrors fabricated via laser ablation [47] enabling efficient coupling to a single free-space mode [41,48]. The radii of curvature of these micromirrors are $\sim 10\,\mu\mathrm{m}$ resulting in a beam waist of $\sim 1\,\mu\mathrm{m}$. We integrate a high-quality single-crystalline diamond micromembrane [$\sim 20 \times 20 \times 0.8\,\mu\mathrm{m}^3$, Fig. 1(b)] into the cavity using a micromanipulator [49,50] (see Appendix A).

For conventional Fabry–Perot resonators, the resonance wavelength changes linearly with the mirror separation t_a. However, the presence of a diamond membrane with thickness t_d significantly alters this linear mode structure. The hybridization of modes confined in the air and diamond layers of the resonator manifests in avoided crossings [35,50–54]. The cavity resonance frequencies depend on both the separation of the two mirrors and the thickness of the diamond at the location of the cavity mode. One of the main advantages of our cavity platform is the *in situ* tuning capability. Both the separation of the mirrors and the lateral position of the cavity mode with respect to the diamond membrane can be controlled via a stack of piezoelectric nanopositioners (attocube ANPx51, ANPz51). The diamond membrane exhibits a slight thickness gradient introduced during the thinning of the diamond [55–57]. It was shown in the past that this thickness gradient is
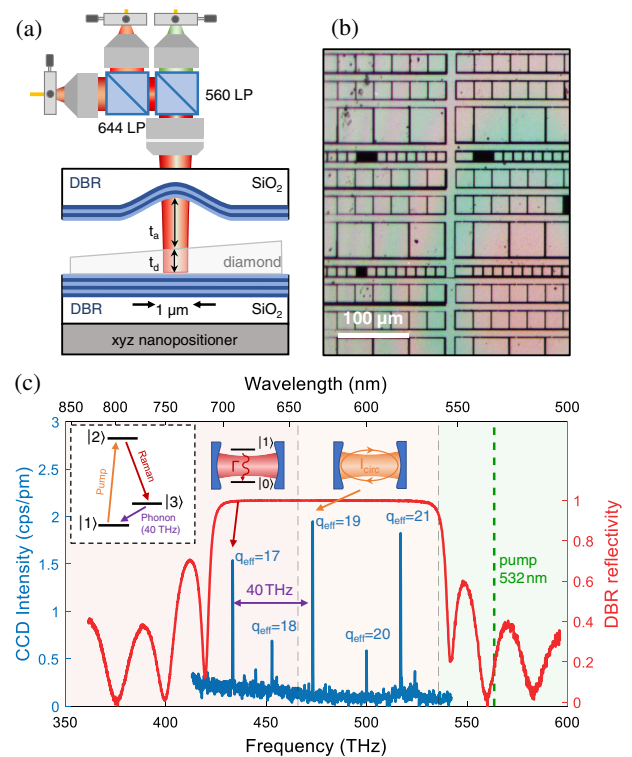

Fig. 1. (a) Schematic of the plano–concave Fabry–Perot microcavity. The cavity is formed by two fused silica (SiO$_2$) substrates coated with a distributed Bragg reflector (DBR). One of the substrates contains spherical micro-indentations resulting in a Gaussian resonator mode with a small beam waist ($\sim 1\,\mu\mathrm{m}$). Piezoelectric nanopositioners allow for spatial and spectral tunability of the cavity mode. The wedged diamond membrane enables the diamond thickness within the cavity mode to be changed by lateral positioning. The thickness gradient of the diamond is exaggerated for clarity. The collimated green and tunable red lasers are combined via two long-pass (LP) dichroic mirrors (splitting wavelengths at 560 nm and 644 nm) and coupled into the cavity via a mode-matching objective lens. (b) Optical microscope white-light image of a large array of fabricated diamond micromembranes. The Newton fringes indicate a variation of the membrane thickness that is introduced during the thinning process using plasma etching. (c) In red: measurement of the reflectivity of the planar DBR revealing a stopband centered at 625 nm with a bandwidth of $\sim 100\,\mathrm{THz}$. In blue: experimental cavity spectrum for a fixed cavity length under 532 nm illumination. The mirror separation is set such that there are two fundamental modes with a splitting of $\sim 40\,\mathrm{THz}$. In this configuration resonant recirculation of a laser resonant with mode $q_{\mathrm{eff}} = 19$ increases the intracavity intensity (denoted by I_{circ}), while the Raman process is enhanced by mode $q_{\mathrm{eff}} = 17$. The differently shaded wavelength regimes are bound by the splitting wavelength of the employed dichroic mirrors. For details, see text. Inset: Raman process, depicted as a three-level system. A photon is converted into a redshifted photon and an optical phonon of fixed frequency.

universal to thinned diamond devices, but that it can also be tuned with reasonable accuracy [56]. Harnessing this gradient, we are able to tune the exact diamond thickness of the membrane in the cavity by adjusting the relative lateral positions of the mirrors. The *in situ* tuning capability allows controlling both the absolute frequency as well as the relative splitting of the resonator modes.

Excitation of the first-order Raman process (here, the Stokes process) in diamond can be modeled as a three-level atom-like system [inset Fig. 1(c)] involving a ground state $|1\rangle$, a virtual state $|2\rangle$, and a meta-stable state $|3\rangle$. A pump laser excites the ground-state population from $|1\rangle$ to $|2\rangle$. The system decays via state $|3\rangle$ emitting

a redshifted photon ($|2\rangle \rightarrow |3\rangle$) followed by an optical phonon of fixed frequency ($\sim 1,332$ cm^{-1} [38], ~ 40 THz, $|3\rangle \rightarrow |1\rangle$).

By coupling both the pump and the Stokes photons to a cavity mode, the Stokes process can be strongly enhanced [58]. Resonant recirculation of the pump laser increases the intracavity intensity, denoted by I_{circ} in Fig. 1(c), while a cavity mode resonant with the Raman transition enhances the creation of Stokes photons [41]. Careful tuning of the mirror separation t_a and the diamond thickness t_d allows the double-resonance condition to be established for a wide range of pump wavelengths in the visible wavelength regime. Upon changing the pump wavelength, t_d and t_a need to be adjusted such that one cavity mode remains resonant with the pump laser; another mode is red-detuned with respect to the pump by exactly the Raman shift (see Appendix D).

The operation wavelength range of the cavity is given by the reflective stopband of the distributed Bragg reflector (DBR), which we determine using a white-light transmission measurement [41]. Figure 1(c) displays the stopband of the planar bottom mirror centered around $\lambda_{\text{c,bot}} = 625$ nm; the reflectivity is more than 99% over a bandwidth of ~ 100 THz. The top mirror has similar properties but with a stopband centered at $\lambda_{\text{c,top}} = 629$ nm. To characterize the mode structure of the cavity, we couple a green laser at 532 nm into the cavity through the curved top mirror via a dichroic mirror (Semrock, FF560-FDi01). We tune the mirror separation by applying a voltage to the z-piezo using a highly stable voltage source (Basel Precision Instruments SP 927). Background photoluminescence (PL) from the diamond acts as an internal light source and couples to the different resonator modes [41]. Crucially, the green laser is outside the reflective stopband of the mirror, and can thus excite PL independent of the cavity length.

3. RESULTS

We set the mirror separation such that the splitting between the modes with effective mode numbers $q_{\text{eff}} = 17$ and $q_{\text{eff}} = 19$ corresponds to the Raman shift in diamond [$\Delta \nu_R \sim 40$ THz, inset Fig. 1(c)]. We define the effective mode number q_{eff} by the number of half-wavelengths between the two mirrors, i.e., within the air gap and the diamond layer, $q_{\text{eff}} \lambda/2 \approx t_a + n_d t_d$. A small deviation from integer values of q_{eff} is caused by field penetration into the DBR mirrors [59,60]. Figure 1(c) displays a PL spectrum collected through the top mirror using a grating-based spectrometer with 300 grooves/mm (Princeton Instruments Acton SP2500). We model the spectrum using a one-dimensional transfer-matrix calculation and infer the mirror separation and diamond layer thickness to be $t_a = 4.18$ µm and $t_d = 756$ nm, respectively. We note that the values of t_a and t_d carry a potential source of systematic error (see Appendix B).

Next, we verify that we are able to establish the double-resonance condition. To this end, we couple an additional tunable external cavity diode laser into the cavity (Toptica DL Pro 635, $\lambda_{\text{pump}} = 630 \cdots 640$ nm, $\delta \nu \leq 500$ kHz) by adding a dichroic mirror to our optical setup (cut off at 644 nm, AHF F48-644). We set the laser wavelength to be resonant with mode $q_{\text{eff}} = 19$ at $\lambda_{\text{pump}} = 632.99$ nm. The resulting Raman scattered light is at a wavelength of $\lambda_R = (1/\lambda_{\text{pump}} - \Delta \nu_R/c)^{-1} = 691.25$ nm, where c is the speed of light.

In the following, we denote the effective mode number of the cavity mode that is close in wavelength to the tunable red pump laser (λ_{pump}) as q_p and the corresponding wavelength as λ_p^{cav}; and the effective mode number of the cavity mode close in

wavelength to that of the Raman photon (λ_R) as q_S and its associated wavelength as λ_S^{cav}. An analogous notation is adapted for the corresponding frequencies ν.

We then tune the mirror separation and record spectra from the cavity (Fig. 2). The background PL excited by the green laser couples to the cavity modes with effective mode numbers $q_S = 16 \ldots 18$ and wavelengths in the range of $\lambda = 670 \ldots 700$ nm, which redshift with increasing mirror separation. When the tunable red pump laser at $\lambda_{\text{pump}} = 632.99$ nm is resonant with the $q_p = 18 \ldots 20$ modes for relative mirror separations ΔL_{cav} of -317.0 nm, 0 nm, and $+317.0$ nm, narrow peaks appear in the spectrum at CCD pixels corresponding to $\lambda = 691.19$ nm and $\lambda = 691.32$ nm, as highlighted in the insets of Fig. 2 matching well the predicted $\lambda_R = 692.25$ nm. As displayed in the respective linecuts for $\Delta L_{\text{cav}} = -317$ nm, the cavity mode with $q_S = 16$ appears at a too long wavelength, while for $\Delta L_{\text{cav}} = +317$ nm, the wavelength of $q_S = 18$ is too short. Only at $\Delta L_{\text{cav}} = 0$ nm are both the pump and the Stokes field each resonant with a cavity mode.

Similarly, the linecut at $\lambda = 691.19$ nm clearly shows that the cavity resonances for $q_S = 16$ and $q_S = 18$ appear at smaller (-345.6 nm) and larger relative mirror separations ($+345.6$ nm) than the Raman peaks, respectively. Only for a mirror separation of $t_a = 4.18$ µm are λ_{pump} and λ_R simultaneously resonant with the cavity (within the spectrometer resolution) for $q_p = 19$ and $q_S = 17$. For this double-resonance condition, the signal intensity is increased by over three orders of magnitude compared to the other peaks.

Next, we characterize in more detail the exact detuning dependence of the double-resonance condition by tuning the pump laser. For the remainder of this paper, excitation is carried out using the tunable red laser only. Its wavelength (frequency) will be denoted as λ_{pump} (ν_{pump}). We modulate the cavity length continuously and exploit the fact that Raman signal is generated only when a cavity mode q_p is resonant with the pump laser, $\nu_{\text{pump}} = \nu_p^{\text{cav}}$. Using this technique, it is not necessary to keep the cavity at one particular length—this circumvents any problems caused by either drift or acoustic and thermal noise.

Figure 3(a) displays a set of PL spectra recorded using a high-resolution grating with 2,160 grooves/mm. We vary $\nu_{\text{pump}} = \nu_p^{\text{cav}}$ ($\lambda_{\text{pump}} = \lambda_p^{\text{cav}}$) from 468.475 THz (639.932 nm) to 474.471 THz (631.845 nm). We find that for the pump frequency $\nu_{\text{pump,dres}} = 472.434$ THz, the double-resonance condition is fulfilled: $\nu_R = \nu_S^{\text{cav}} = \nu_{R,\text{dres}} = 432.508$ THz. These values are different from those given in Fig. 2 due to a slightly different lateral position of the cavity mode corresponding to a different diamond thickness, which we will discuss in detail in a subsequent section. We determine a Raman shift of $\Delta \tilde{\nu}_R = \nu_{\text{pump,dres}}/c - \nu_{R,\text{dres}}/c = 1,331.8$ cm^{-1} ($\Delta \nu_R = c \Delta \tilde{\nu}_R = 39.927$ THz), in good agreement with the previously reported value, $\sim 1,332$ cm^{-1} [37,61,62]. We plot the peak Raman counts for different detunings of the pump laser from the double-resonance condition, $\nu_{\text{pump}} - \nu_{\text{pump,dres}}$ [projected blue points in Fig. 3(a)]. We find that these peak counts follow a Lorentzian with FWHM linewidth of 519.8 GHz [58]. The corresponding projected Raman amplitude is fitted well by a Lorentzian with FWHM linewidth of 502.9 GHz [projected red points in Fig. 3(a)].

We fit the individual spectra for different detunings of the pump laser (with respect to the double-resonance frequency
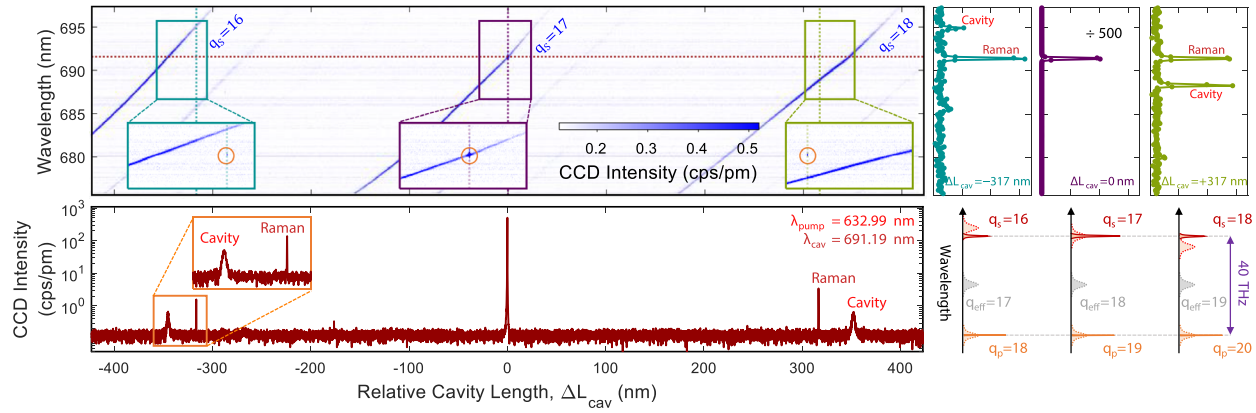
Fig. 2. Demonstration of cavity-enhanced doubly resonant Raman scattering. (top) Optical spectra as a function of relative cavity length reveal the cavity mode structure. Here, a laser at 532 nm excites background PL in the diamond, and a narrowband diode laser at $\lambda_{pump} = 632.99$ nm drives Raman scattering. For $q_p = 19$ and $q_S = 17$, the pump and Raman scattered lights are resonant simultaneously, i.e., the double-resonance condition is met. (bottom) Linecut at $\lambda = 691.19$ nm highlighting the strong signal enhancement of doubly resonant Raman scattering. (right) Linecuts at different relative cavity lengths ΔL_{cav} showcasing the double resonance for $q_p = 19$ and $q_S = 17$. At shorter ΔL_{cav}, the mode splitting between $q_p = 18$ and $q_S = 16$ is too large for the Raman scattered light to be resonant, while for larger ΔL_{cav}, the mode splitting between $q_p = 20$ and $q_S = 18$ is too small. For more details, see text.

$\nu_{pump,dres}$) to the product of two Lorentzians describing the cavity mode at ν_S^{cav} (FWHM $\delta \nu_S^{cav}$) and the gain bandwidth of the Raman scattering process at ν_R [FWHM $\delta \nu_R$, Fig. 3(b)]. These fits allow the peak positions and linewidths to be extracted [41]. Figures 3(c) and 3(d) display the results of these fits. Over the tuning range of the pump laser, the detuning between ν_S^{cav} and ν_R varies from -319.7 GHz to 526.7 GHz. The linewidth of the Raman gain for the different fits is $\delta \nu_R = (48.3 \pm 1.6)$ GHz corresponding to $Q_R = 8,960 \pm 290$. This Raman linewidth agrees well with previously reported values (40.8 … 47.8 GHz) [39–41], indicating low strain in the diamond membrane. The linewidth of the cavity mode closest to ν_R at ν_S^{cav} decreases from $\delta \nu_S^{cav} = (167.3 \pm 0.8)$ GHz to (47.0 ± 0.4) GHz for increasing $\nu_{pump} = \nu_p^{cav}$, which is expected from the increase in reflectivity on approaching the stopband center of the DBR mirror coatings. The corresponding Q-factor increases from $Q_S = 2,570 \pm 90$ to $9,250 \pm 90$. In the double-resonance condition, the Q-factor of the Stokes cavity mode is $Q_{S,dres} = 6,650 \pm 50$.

We now turn to discussing the effect of the diamond thickness in more detail. The presence of the diamond membrane in the cavity significantly alters the cavity mode dispersion with respect to conventional Fabry–Perot cavities. Conceptually, the cavity mode structure can be described using a coupled two-cavity model: one cavity is confined to the diamond bounded by the bottom DBR and the diamond–air interface; the other cavity is confined to the air bounded by the diamond–air interface and the top DBR [33,41,63]. The finite contrast in refractive index across the diamond–air interface couples the two cavities, resulting in a hybridized mode structure, manifested by the emergence of avoided crossings [35]. The resonance frequencies depend on both t_a and t_d at the position of the cavity mode. Figure 4 displays a one-dimensional transfer-matrix calculation (Essential Macleod) of the cavity mode structure, using the mirror structure extracted from Fig. 1(c). These calculations confirm that the locations of the avoided crossings in the mode structure depend on the choice of diamond thickness t_d.

Next, we demonstrate the possibility to tune the double-resonance condition by changing the thickness of the diamond layer within the cavity mode *in situ* [Fig. 5(a)]. To this end, we laterally displace the cavity mode with respect to the diamond membrane, exploiting the small thickness gradient [Fig. 1(a)]. Over the lateral fine-tuning range of the nanopositioner (travel range ~ 4 µm), the double-resonance condition can be tuned from $\nu_{pump,dres} = 471.44$ THz to 472.29 THz ($\nu_{R,dres} = 431.51$ THz to 432.36 THz), a continuous tuning range of 0.85 THz. Considering that the width of the double-resonance gain profile is > 500 GHZ, this would enable a $>$ THz continuous tuning range of the lasing frequency as will be discussed below.

To extract the exact diamond thickness, we perform one-dimensional transfer-matrix-based simulations of the cavity mode structure. For these simulations, we use the exact mirror structure obtained from fitting the mirror stopband (Fig. 1(c) [33,41]), and sweep the width of the air gap t_a and the diamond thickness t_d for fixed wavelengths λ_p^{cav} and λ_S^{cav}. The double-resonance condition is met whenever the modes for λ_p^{cav} cross the modes for λ_S^{cav}. Figure 5(b) shows a transfer-matrix simulation for $\lambda_p^{cav} = 634.57$ nm and $\lambda_S^{cav} = 693.15$ nm [extracted from Fig. 3(c)]. Here, the two cavity modes overlap for $t_a = 4.18$ µm and $t_d = 755$ nm, which well reproduces the spectrum in Fig. 1(c). We note that we neglected dispersion in the diamond membrane since the error is significantly smaller than the uncertainty of the transfer-matrix simulation (see Appendix B).

We extract t_d for all measurements displayed in Fig. 5(a) and plot t_d versus lateral displacement of the cavity mode [Fig. 5(c)]. To calibrate the lateral displacement, we use the edges of the diamond (~ 18 µm) measured with a laser scanning confocal microscope (Keyence Corporation) as a reference. We find a thickness gradient $|\frac{\Delta t_d}{\Delta x}| = (0.16 \pm 0.10)$ nm/µm. This gradient agrees well with the thickness variation we extract from analyzing thin-film interference of the diamond membrane (see Appendix A). As shown in Fig. 5(d), we observe a linear shift of λ_S^{cav} with t_d. From our simulations, we find that for the right combination of t_a and t_d, the double-resonance condition can be tuned continuously across the whole mirror stopband corresponding to a continuous tuning range of tens of THz (see Appendix D).

Next, we perform double-resonance measurements for different pump powers P_{pump} (as measured before the sample objective)
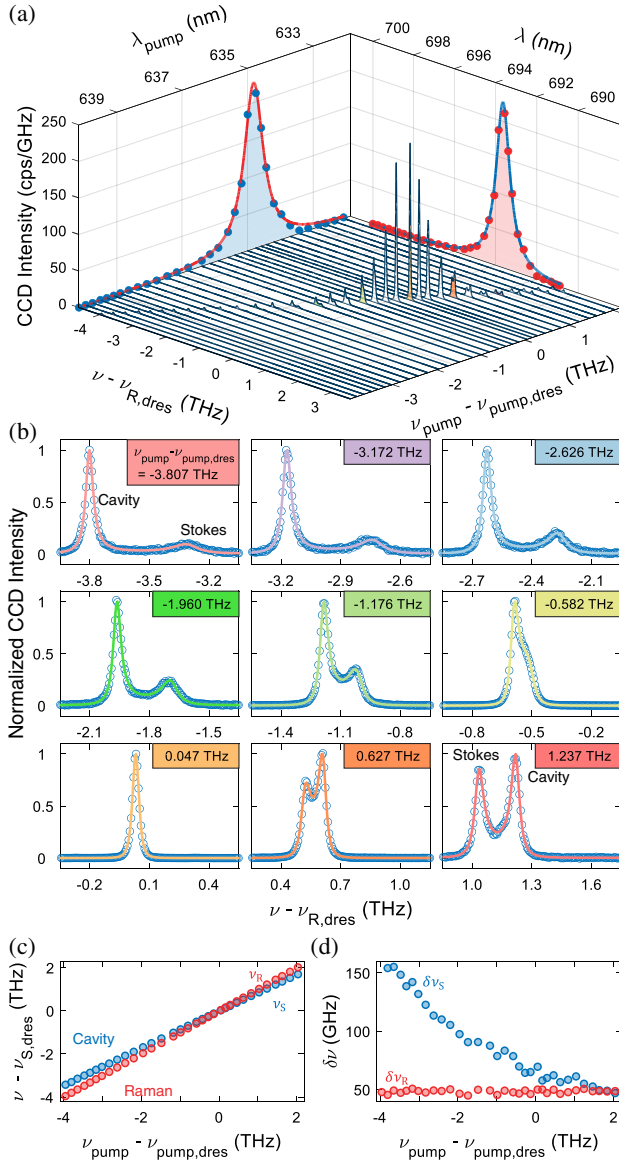
Fig. 3. (a) Series of cavity spectra for different detunings of the pump laser from the double-resonance condition $\nu_{\text{pump}} - \nu_{\text{pump,dres}}$. The cavity spectra comprise the Raman signal at ν_R and the closest cavity mode at ν_S^{cav}. We fit the amplitude of the Raman signal for every value of $\nu_{\text{pump}} - \nu_{\text{pump,dres}}$ with a Lorentzian (projected blue points) with linewidth of 519.8 GHz. The center frequency of the fit indicates that the double-resonance condition is satisfied when $\nu_{R,\text{dres}} = 432.508$ THz for $\nu_{\text{pump,dres}} = 472.434$ THz. (b) Individual cavity spectra obtained with different pump frequencies can be fitted well using a model based on two multiplied Lorentzians centered at the Stokes frequency $\nu_R - \nu_{R,\text{dres}}$ and the frequency of the adjacent cavity mode $\nu_S^{\text{cav}} - \nu_{R,\text{dres}}$. (c) Peak position of the cavity (ν_S^{cav}) and Raman scattering (ν_R) as a function of pump frequency ν_{pump} relative to the double resonance condition at $\nu_{\text{pump, dres}}$ and $\nu_{R,\text{dres}}$. (d) Linewidth of the cavity ($\delta\nu_S^{\text{cav}}$) and the Raman gain ($\delta\nu_R$) versus pump frequency $\nu_{\text{pump}} - \nu_{\text{pump, dres}}$.

[Figs. 6(a) and 6(b)]. Up to the largest available pump power in the experiment, the intensity increases linearly: there is no superlinear dependence presaging Raman lasing.

We estimate the threshold power required to establish Raman lasing using classical coupled mode equations [64,65]. Lasing occurs when the round-trip gain equals the round-trip loss. Assuming that both the pump laser and the Raman light are
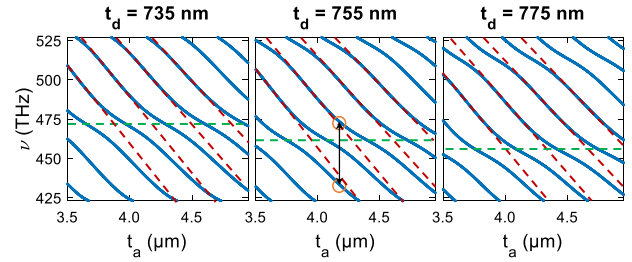

Fig. 4. One-dimensional transfer-matrix calculation of the cavity mode structure, i.e., resonance frequencies for different mirror separations t_a, for different diamond thicknesses t_d. The nonlinear mode dispersion arises as a consequence of hybridization of cavity modes resonant with the air gap (indicated by the dashed burgundy line) and the diamond (dashed green line). The hybridization leads to avoided crossings whose positions depend on the exact diamond thickness. The central panel shows the mode structure for the extracted diamond thickness ($t_d = 755$ nm) from Fig. 5(b). The orange circles indicate a pair of cavity modes whose frequencies are separated by the Raman shift of $\Delta\nu_R \sim 40$ THz (black arrow).
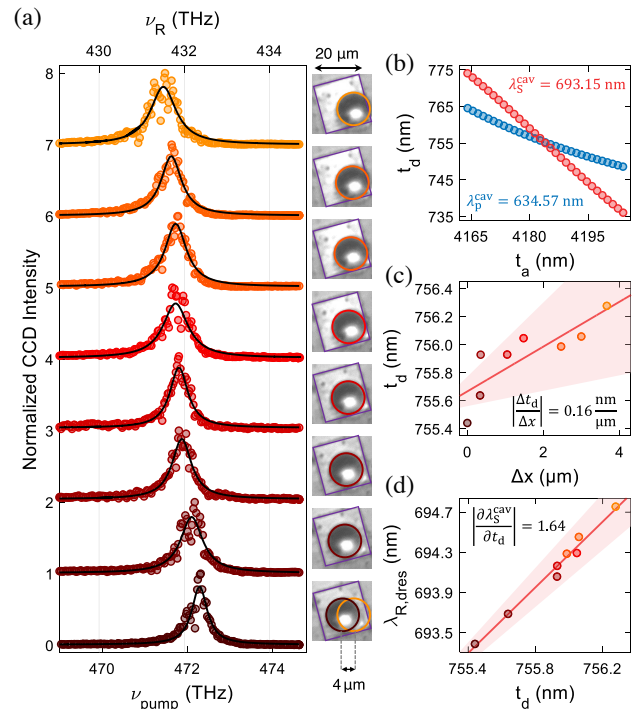

Fig. 5. (a) Demonstration of the tunability of the double-resonance condition. Owing to the thickness gradient, shifting the diamond laterally changes the diamond thickness in the cavity and subsequently the condition for double resonance. The images to the right show the relative position of the cavity, as indicated by the circles, with respect to the edges of the diamond (purple rectangle). The bright feature in the center of the cavity stems from the reflection of the excitation laser. (b) The diamond thickness and the width of the air gap are extracted from one-dimensional transfer-matrix simulations. The double-resonance condition is satisfied when the pump mode (blue) and the Stokes mode (red) cross. For $\lambda_P^{\text{cav}} = 634.57$ nm and $\lambda_S^{\text{cav}} = 693.15$ nm, we extract $t_d = 755$ nm and $t_a = 4.18$ μm. (c) Lateral displacement of the cavity mode plotted against diamond thickness t_d. Here, the relative position of the cavity mode is calculated with respect to the corners of the diamond. Extracting the diamond thickness from the double-resonance measurements in (a) gives a thickness gradient of 0.16 nm/μm. (d) Linear shift of the double-resonance condition with the diamond thickness resulting in a redshift of the Stokes wavelength.
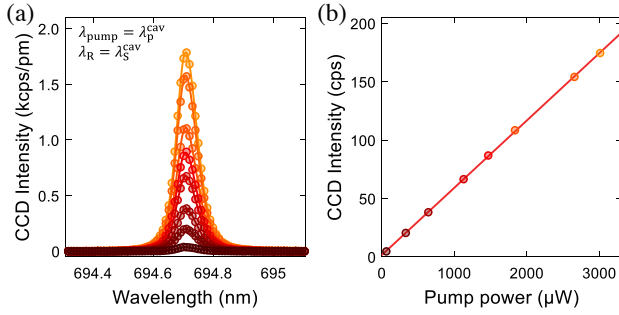
Fig. 6. (a) Spectrally resolved cavity signal with increasing pump power in the double-resonance condition. (b) Integrated intensity of the peaks in (a) as a function of pump power. The linear behavior suggests that no lasing occurs.

resonant with the cavity, $\lambda_{\text{pump}} = \lambda_{\text{p}}^{\text{cav}}$ and $\lambda_{\text{R}} = \lambda_{\text{S}}^{\text{cav}}$, the lasing threshold P_{th} can be calculated via (see Appendix F):

$$P_{\text{th}} = \frac{1}{\eta} \frac{2 n_{\text{S}} n_{\text{p}} \pi^2}{\lambda_{\text{S}}^{\text{cav}} \lambda_{\text{p}}^{\text{cav}} g_{\text{R}}^{\text{B}}} \frac{V_{\text{R}}(Q_{\text{S}} + Q_{\text{R}})}{Q_{\text{S}}^2 Q_{\text{p}}}. \tag{1}$$

Here, $\lambda_{\text{p(S)}}^{\text{cav}}$, $n_{\text{p(S)}}$, and $Q_{\text{p(S)}}$ are the wavelengths, refractive indices, and Q-factors for the cavity modes resonant with the pump laser and the Raman light, respectively. Q_{R} is the quality factor corresponding to the bandwidth of the Raman gain. The bulk Raman gain coefficient in the employed pump wavelength range is $g_{\text{R}}^{\text{B}} \sim 40$ cm/GW [66]. The power incoupling efficiency η and the quality factor of the pump mode can be extracted from the cavity transmission measurement displayed in Fig. 8 [67,68]. From the dip in reflection, we infer a power incoupling efficiency of $\eta_{\text{C}} = 1 - P_{\text{R}}/P_0 = 0.45$, while the quality factor of the pump mode Q_{p} is determined to be 296,900±600.

We model specifically the possibility of Raman lasing in the cavity used in all the experiments. Using a one-dimensional transfer-matrix model along with Gaussian optics, we estimate a Raman mode volume of $V_{\text{R}} = 108 \ \mu\text{m}^3$ (see Appendix E). Taking $n_{\text{p(S)}} = n_{\text{dia}} = 2.4$, we find $P_{\text{th}} = 189$ mW. This relatively low threshold power constitutes a reduction in threshold power by more than an order of magnitude with respect to a bulk Raman laser in the visible [69–71].

We acknowledge that the current experiment does not feature the best combination of frequencies for Raman lasing—the Stokes frequency lies close to the edge of the stopband such that its cavity mode has a modest Q-factor—but the experimental cavity has the virtue of having been extensively investigated. Accessing more suitable wavelengths close to the center wavelength of the mirror stop bands at $\sim$625 nm, which would maximize the figure of merit $(Q_{\text{S}} + Q_{\text{R}})/(Q_{\text{S}}^2 Q_{\text{p}})$ [Eq. (1)], was not possible since we do not have access to a tunable laser around 600 nm.

In general, diamond is particularly suited for the creation of a Raman laser owing to the combination of a large Raman gain ($\sim$75 GW·cm^{-1} at 532 nm) [37] and a large Raman shift ($\sim$1,332 cm^{-1}) [38]. This large Raman shift enables coherent radiation to be created at exotic wavelengths, e.g., in the yellow band [69,70,72–75], for which no ideal solution exists in terms of cost, convenience, and output power. The wide bandgap of diamond prevents free carrier absorption, thus minimizing optical losses, allowing for operation across a large range of wavelengths, from the ultraviolet [76] across the visible [70,75,77] and infrared [78–86], all the way to the mid-infrared [81]. However, current implementations based on bulk diamond crystals are limited

by their high threshold pump powers, typically on the order of several Watts. As demonstrated here, the threshold pump power can be drastically reduced in an optical microcavity, where resonant recirculation of the pump beam significantly enhances the intensity-dependent Raman gain. Furthermore, simultaneous coupling of the Raman field to a second cavity mode boosts the efficiency of stimulated emission.

It should be noted that no population inversion is required for stimulated Raman scattering and hence the creation of a Raman laser [87]. Importantly, the gain of the Raman process is maximized by strong confinement and overlap of the pump and Raman modes, suggesting the use of fundamental resonator modes. Based on this doubly resonant configuration, low-threshold Raman lasers were demonstrated in many platforms such as silica [11,12], silicon [88–91], lithium niobate [92], silicon carbide [93], and aluminum nitride [94]. Recently, even molecules adsorbed to silica microtoroids emerged as promising gain media [26]. Advances in diamond nanofabrication enabled the demonstration of integrated diamond Raman lasers using ring resonators at infrared [8] and near-visible [9] wavelengths with threshold powers of $\sim$20 mW. Further progress, however, is limited by loss due to fabrication-induced roughness and the lack of widely available diamond films with homogeneous thickness.

We predict that with realistic improvements, our platform has the potential to feature threshold powers in the $\sim$mW range (see Appendix G) and that, based on its wide-range tunability, it could pave the way to the creation of a universal, low-threshold, frequency shifter for coherent radiation.

4. CONCLUSION

In conclusion, we demonstrate a platform for the widely tunable, doubly resonant enhancement of Raman scattering from diamond based on a tunable open-access microcavity. The *in situ* tuning capability of our device provides a convenient way to establish a double-resonance condition in which both pump and Raman wavelengths are each resonant with a cavity mode. The key novelty is the exploitation of a slight thickness gradient in the incorporated diamond membrane. This enables the doubly resonant configuration to be achieved over a wide tuning range, more than 1 THz. These results, together with the high quality factors of the cavity in the visible wavelength range, suggest that Raman lasing can be achieved with the present system. With the experimentally determined parameters, we predict a lasing threshold of 189 mW, a reduction by more than an order of magnitude compared to bulk Raman lasers [95]. We anticipate that with realistic improvements of our platform, sub-mW Raman lasing thresholds can be achieved. Importantly, we predict that there are configurations where mode-hop-free tuning of the double-resonance condition over tens of THz is possible, limited only by the spectral widths of the reflective stop bands of the mirrors. Finally, we note that due to the generic design of our platform, other wide-bandgap Raman laser materials such as aluminum nitride [94] can readily be incorporated into our device. A wider point is that the integration of materials exhibiting a strong $\chi^{(2)}$ nonlinearity such as silicon carbide [14,96], lithium niobate [97], or gallium phosphide [22,23] could enable low-threshold frequency conversion using other nonlinear processes, for instance, second harmonic generation or sum- and difference-frequency mixing.

APPENDIX A: OPEN MICROCAVITY PLATFORM

The core of this experiment is the tunable, planar–concave Fabry–Perot microcavity [44,45] with an embedded diamond micromembrane, depicted schematically in Fig. 1(a). The microcavity comprises two fused silica substrates exhibiting highly reflective dielectric mirror coatings (ECI evapcoat). Prior to applying the coating, we fabricate an array of spherical micro-indentations via CO_2 laser ablation [47] in one of the substrates. The micro-indentations feature small radii of curvature $R_{cav} \sim 10 \ \mu m$ and depths $d \sim 1.5 \ \mu m$. We employ 14 (15) $\lambda_c/4$ layers of a SiO_2/Ta_2O_5 DBR for the curved top (planar bottom) mirrors. From a white-light transmission measurement [33,41,98], the center of the stopband of the bottom mirror is determined to be $\lambda_c = 625$ nm [Fig. 1(c)]. Using a transfer-matrix-based refinement algorithm (Essential Macleod) we can reconstruct the reflection spectrum utilizing an individual layer-thickness tolerance of 3% with $n_{SiO_2} = 1.46$ and $n_{Ta_2O_5} = 2.11$. Using the same approach, we find $\lambda_c = 629$ nm for the top mirror.

Starting with commercially available high-purity, $\langle 100 \rangle$-cut single-crystal diamond (Element Six, $d \sim 40 \ \mu m$), we fabricate membranes via inductively coupled reactive-ion etching and electron-beam lithography [49,55,99]. Figure 7(a) displays a scanning electron micrograph of a region with dimensions $\sim 600 \ \mu m \times 800 \ \mu m$ thinned down to $\sim 5 \ \mu m$. The quartz mask is subsequently swapped to a mask with a narrower opening ($\sim 500 \ \mu m$) to avoid detaching of the membrane due to a trenching effect close to the edge of the quartz mask. When the diamond is thinned down to a sub-μm thickness, Newton fringes emerge based on thin-film interference. By analyzing the spacing of the fringes, we find that the thinnest region of the membrane has a thickness variation as low as 0.5 nm/μm in the y direction and 1.1 nm/μm in the x direction in the center [Fig. 7(b)]. To fabricate the micromembranes, the diamond is flipped and the thin region of the diamond is structured via electron-beam lithography using a hydrogen silsesquioxane negative electron beam resist and subsequent plasma etching. We then transfer a membrane with typical dimensions $\sim 20 \times 20 \times 0.8 \ \mu m^3$ to the planar mirror using a micromanipulator [49,50] [Fig. 1(b)].
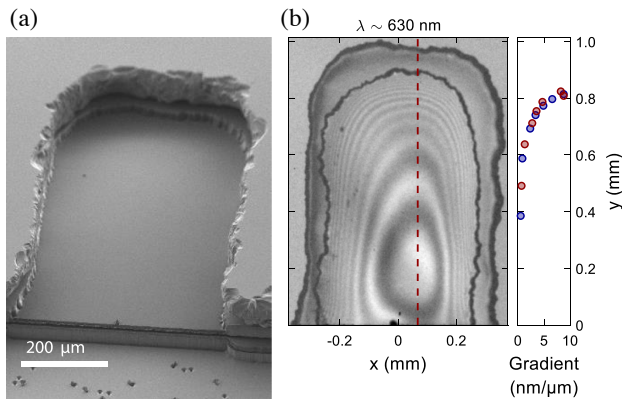

Fig. 7. (a) Scanning electron microscopy image obtained after the first thinning step of a diamond plate. (b) Red channel (~ 630 nm) of an optical microscope white-light image of the final membrane structure. By analyzing the spacing between the Newton fringes emerging due to thin-film interference, the thickness gradient of the diamond membrane can be determined. The plot on the right displays the thickness gradient extracted from measuring the spacing between crests (blue) and troughs (red) of the interference pattern along the linecut marked by the red dashed line.
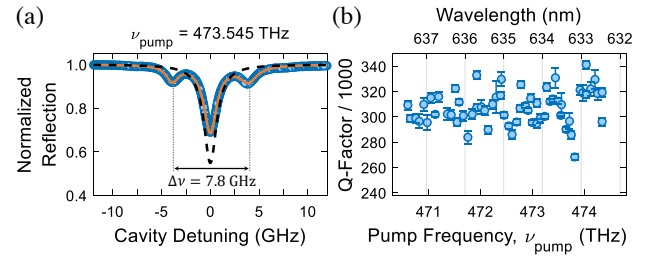

Fig. 8. (a) Q-factor measurement for $\nu_p^{cav} = c/\lambda_p^{cav} = 473.545$ THz. Sidebands created by an EOM at $\nu_{pump} \pm 3.9$ GHz act as a frequency ruler to extract the cavity linewidth. (b) Q-factor as a function of cavity resonance frequency.

The bottom mirror is mounted on a stack of xyz-piezoelectric nanopositioners (attocube, $2 \times ANPx51$ and ANPz51) and placed inside a home-built titanium "cage"; the top mirror is rigidly attached to the top of the cage [33]. By applying a voltage to the nanopositioners, the bottom mirror can be moved in all three dimensions with respect to the top mirror, offering both spatial and spectral tunability [50]. Finally, the titanium cage is mounted on top of a high-precision mechanical stage (Newport, M-562-XYZ) to enable the cavity output to be coupled to external detection optics [41]. We use a narrowband tunable red diode laser as the pump laser (Toptica DL Pro 635, $\lambda_{pump} = 630 \cdots 640$ nm, $\delta\nu \leq 500$ kHz). We determine the wavelength of the laser using a high-precision wavelength meter (HF-Angstrom WS/U-30U) calibrated with a stabilized helium neon laser. This tunable pump laser is spectrally filtered (Semrock, FF01-637/7-25 and FF01-650/SP-25) and then coupled into the cavity using an objective of moderate numerical aperture (Microthek, $20\times$, NA = 0.4) [41]. The Stokes signal is collected via the same objective in a backscattering geometry [Fig. 1(a)]. A combination of a dichroic mirror (cutoff 644 nm, AHF F48-644) and a long-pass filter (Semrock, BLP02-635 R-25) is used to filter the excitation laser from the signal. The Stokes signal is then coupled into a single-mode detection fiber (Thorlabs, 630-HP) and recorded with a spectrometer (Princeton Instruments, Acton SP2500).

We determine the quality factor of the pump mode of the cavity, Q_p, following the method reported in Ref. [33]. To extract the cavity linewidth, we keep the laser frequency ν_{pump} fixed while scanning the cavity length and monitoring the reflected light on a photodiode. An electro-optic modulator (EOM, Jenoptik PM635) is used to create laser sidebands at $\nu_{pump} \pm 3.9$ GHz, thereby providing a frequency ruler to extract the cavity linewidth. Figure 8(a) shows the reflected signal averaged over 200 scans for $\nu_{pump} = 473.233$ THz. Assuming a linear response of the piezo across the resonance, we extract a cavity mode FWHM linewidth of $\delta\nu_p^{cav} = (1.593 \pm 0.004)$ GHz corresponding to a quality factor of $Q_p = 297{,}000 \pm 800$. Figure 8(c) shows the dependence of Q_p on the cavity resonance frequency ν_p^{cav}.

APPENDIX B: SYSTEMATIC UNCERTAINTY IN THE AIR AND DIAMOND THICKNESS

We briefly discuss two sources of systematic errors. In this work, the values of t_a and t_d are extracted from transfer-matrix simulations using the reconstructed mirror structure extracted from Fig. 1(c). We note that the 3% thickness tolerance for each layer, amounting to 2.2 nm and 3.2 nm for the high- and low-index material, respectively, introduces a potential systematic error

upon extracting t_a and t_a from these simulations. However, as all simulations are performed using the same mirror structure, this systematic error will be the same for all calculations—relative values of t_a and t_d are determined with high precision. To quantify this systematic error, we repeat the simulation in Fig. 5(b), and extract $t_a = 4.18^{+0.01}_{-0.03}$ μm and $t_d = 756^{+12}_{-1.9}$ nm, where the high and low bounds are estimated by accounting for the extreme tolerance in each mirror layer thickness.

Similarly, dispersion in the diamond membrane introduces another source of systematic error. Accounting for dispersion in Fig. 5(b) yields a maximum uncertainty $\Delta t_a = 1.9$ nm and $\Delta t_d = 0.8$ nm—significantly smaller than the uncertainty associated with the transfer-matrix simulations.

APPENDIX C: ESTABLISHING THE DOUBLE-RESONANCE CONDITION

In Fig. 2(a), we establish the double-resonance condition by spectrally investigating the mode dispersion with increasing t_a. A faster way to confirm that the double-resonance condition is satisfied is displayed in Fig. 9. Here, we couple only the diode laser at λ_{pump} into the cavity and record the cavity transmission using a photodiode located beneath the bottom mirror. The transmission spectrum reveals several peaks at mirror separations where the pump laser is resonant with the cavity. These peaks are associated with fundamental and higher-order cavity modes. Simultaneously, we measure the cavity emission at wavelengths >644 nm using a single-photon-counting module. A strong signal is observed only when λ_{pump} is resonant with mode $q_p = 19$, while at the same time λ_R is resonant with $q_S = 17$. The correlation between a peak in transmission (signifying a resonant pump laser) and a strong peak in cavity emission at longer wavelengths (signifying a resonant Raman process) is a clear demonstration that the double-resonance condition is satisfied.

APPENDIX D: TUNING OF DOUBLE-RESONANCE CONDITION

Open-access microcavities offer a convenient tuning mechanism of their resonance frequency simply by changing the separation of the two mirrors (t_a) using a piezoelectric nanopositioner. Importantly, such cavities offer another tuning mechanism where, rather than the width of the air gap, the thickness of the material
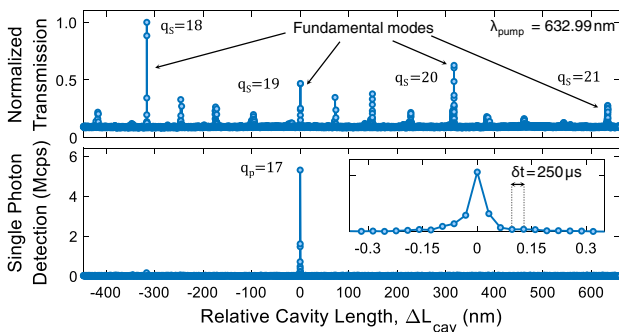
layer is changed *in situ*. Here, a small thickness gradient in the diamond membrane converts a lateral displacement of the cavity mode into a change of the membrane thickness (t_d). Tuning both t_a and t_d allows both the absolute frequency and the spacing of the cavity modes to be controlled. As a consequence, a gradient in the diamond thickness $\left|\frac{\Delta t_d}{\Delta x}\right|$ enables the double-resonance condition to be satisfied for different pairs of frequencies. In Fig. 5(a), we demonstrate experimentally a continuous tuning range of the double-resonance condition by 0.85 THz. This is achieved by changing the diamond thickness by ~0.9 nm, from 755.4 nm to 756.3 nm. To explore this tuning mechanism in more detail, we perform one-dimensional transfer-matrix calculations (Essential Macleod). We calculate the combinations of air-gap width t_a and diamond thickness t_d at which specific wavelengths are resonant. We perform pairwise calculations for the pump cavity mode λ_P^{cav} [solid lines Fig. 10(a)] and the corresponding wavelengths red-shifted by the Raman shift at $\lambda_S^{\text{cav}} = (1/\lambda_P^{\text{cav}} - \Delta \nu_R/c)^{-1}$ [dashed lines Fig. 10(a)] for the range of t_a and t_d accessible with the device presented in the main text. At pairs of t_a and t_d where the solid and dashed line cross, the double-resonance condition is satisfied.

We find that, in principle, the double-resonance condition can be tuned continuously from $\lambda_{\text{pump,dres}} = 625.00$ nm ($\lambda_{R,\text{dres}} = 681.75$ nm) to $\lambda_{\text{pump,dres}} = 649.00$ nm ($\lambda_{R,\text{dres}} = 710.41$ nm) (17.3 THz) by changing the diamond thickness from 751.4 nm to 763.8 nm [green points in Fig. 10(a)]. The experimentally
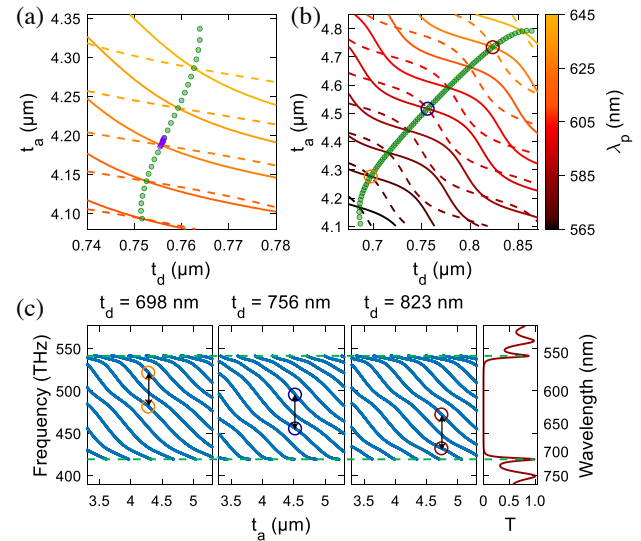

Fig. 10. One-dimensional transfer-matrix calculations of the cavity resonances as a function of t_a and t_d for different combinations of λ_P^{cav} (solid line) and $\lambda_S^{\text{cav}} = (1/\lambda_P^{\text{cav}} - \Delta \nu_R/c)^{-1}$ (dashed line) at specific wavelengths. The double-resonance condition is satisfied when the corresponding solid and dashed lines cross (indicated by same color). By changing the diamond thickness, the condition for the double resonance can be tuned continuously, as indicated by the green circles. (a) Calculations for pairs of t_a and t_d in a range accessible with the device presented in the main text. The calculations suggest a continuous tuning range of 17.3 THz. The experimentally verified tuning is indicated by the purple circles. (b) Optimizing the choice of t_a and t_d enables continuous tuning across the entire reflective stopband, amounting to 72.2 THz. For simplicity, only cavity modes for which continuous tuning is possible are included. (c) Cavity mode structure for the three different diamond thicknesses highlighted in (b). The double-resonance conditions are indicated by the black arrows. The rightmost panel shows the fit of reflective stopband for the bottom mirror extracted from Fig. 1(c).

Fig. 9. Cavity transmission (top) and cavity emission at wavelengths >644 nm measured with a single photon counter (bottom) as a function of cavity length for $\lambda_{\text{pump}} = 632.99$ nm. A cavity signal is observed only when the double-resonance condition is satisfied. The piezo voltage is changed at a rate of 2 mV/ms, which corresponds to a change of cavity length $\Delta L_{\text{cav}}/\text{d}t = 0.13$ nm/ms.

demonstrated tuning range is indicated by the purple points in Fig. 10(a).

By optimizing the choice of t_a and t_d, we find a configuration that, in principle, allows the double-resonance condition to be tuned in a mode-hop-free fashion harnessing the whole stop-band of the mirror [72.2 THz, $\lambda_{\text{pump,dres}} = 565 \cdots 645$ nm, $\lambda_{\text{R,dres}} = 610.98 \cdots 705.62$ nm; see Figs. 10(b) and 10(c)].

APPENDIX E: CALCULATION OF THE EFFECTIVE RAMAN MODE VOLUME

We consider a doubly resonant system ($\omega_p = \omega_{\text{pump}} = \omega_p^{\text{cav}}$ and $\omega_S = \omega_R = \omega_S^{\text{cav}}$). In the following, we omit the "cav" superscripts for concise notation and clarity. The effective Raman mode volume V_R accounts for the spatial overlap of the pump (p) and Stokes (S) cavity modes and can be determined via [64,100]

$$V_R = \frac{\int_{\text{cav}} n_p^2(\vec{r}) |\vec{E}_p(\vec{r})|^2 d^3r \times \int_{\text{cav}} n_S^2(\vec{r}) |\vec{E}_S(\vec{r})|^2 d^3r}{\int_{\text{dia}} n_p^2(\vec{r}) |\vec{E}_p(\vec{r})|^2 \times n_S^2(\vec{r}) |\vec{E}_S(\vec{r})|^2 d^3r}, \quad \text{(E1)}$$

where $\vec{E}_{p(S)}(\vec{r})$ is the pump (Stokes) electric field at position $\vec{r}$. The integrals over the electric field can be calculated following the same approach as reported in Ref. [41]. We approximated the beam waist to be constant $w_{0,I}$ and solve the integral in cylindrical coordinates:

$$\int_{\text{cav}} n^2(\vec{r}) |\vec{E}(\vec{r})|^2 d^3r$$

$$= \int_{\text{cav}} n^2(z) |\vec{E}(z)|^2 dz \int_0^{2\pi} d\phi \int_0^\infty r e^{-r^2/2w_{0,I}^2} dr$$

$$= 2\pi \frac{1}{4} w_{0,I}^2 \int_{\text{cav}} n^2(z) |\vec{E}(z)|^2 dz, \quad \text{(E2)}$$

where $\epsilon_R = n^2$, and $w_{0,I}$ is the intensity beam waist given by [33,101]

$$w_{0,I} = \sqrt{\frac{\lambda}{\pi} \left[\left(t_a + \frac{t_d}{n_d} \right) \times R_{\text{cav}} - \left(t_a + \frac{t_d}{n_d} \right)^2 \right]^{\frac{1}{4}}}. \quad \text{(E3)}$$

Calculating the respective field profiles according to Eq. (E2) reduces Eq. (E1) to

$$V_R = 2\pi \frac{1}{4} \left(w_p^2 + w_S^2 \right)$$

$$\times \frac{\int_{\text{cav}} n_p^2(z) |E_p(z)|^2 dz \times \int_{\text{cav}} n_S^2(z) |E_S(z)|^2 dz}{\int_{\text{dia}} n_p^2(z) |E_p(z)|^2 \times n_S^2(z) |E_S(z)|^2 dz}. \quad \text{(E4)}$$

To calculate the Raman mode volume, we approximate the axial vacuum electric field distribution with a one-dimensional cavity using a transfer-matrix calculation (Essential Macleod). We use the exact mirror structure obtained from fitting the mirror stop-band [Fig. 1(c)] and the combination of t_a and t_d extracted from Fig. 5(b). Figure 11 shows the result of our calculations. We determine the electric field profile for the pump and Stokes fields and then their product by numerical integration. Using $R_{\text{cav}} = 11$ μm and $n_p \simeq n_S = 2.4$, we calculate the beam waists according to Eq. (E3), and find $w_p = 1.05$ μm and $w_S = 1.09$ μm taking the $\lambda_{S,p}^{\text{cav}}$ combination extracted from Fig. 3(c). Finally, we arrive at $V_R = 108.3$ μm³, as quoted in the main text.
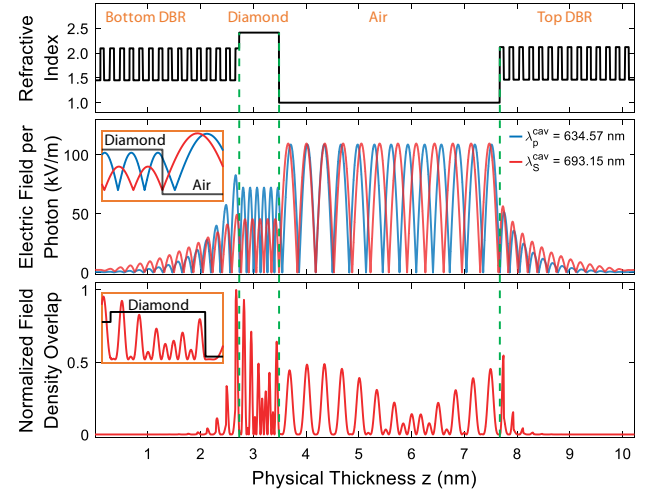

Fig. 11. One-dimensional transfer-matrix simulation of the cavity for $t_a = 4.18$ μm and $t_d = 755$ nm. The top panel shows the refractive index profile as a function of cavity length. The middle panel shows the profile of the pump (blue) and Stokes (red) electric fields. The bottom panel shows the overlap of the energy density calculated according to the denominator in the fraction of Eq. (E1).

APPENDIX F: CALCULATION OF LASING THRESHOLD

To calculate the lasing threshold, we follow the approach presented by Checoury *et al.* [65,102]. We consider a doubly resonant system ($\omega_p = \omega_{\text{pump}} = \omega_p^{\text{cav}}$ and $\omega_S = \omega_R = \omega_S^{\text{cav}}$). As above, we omit the "cav" superscripts. The spacing between the cavity modes is given by $\omega_S = \omega_p - \Delta\omega_R$, and $\Delta\omega_R$ is the Raman shift. The coupled mode equations linking the mean Stokes (N_S) and pump photon numbers (N_p) are given by

$$\frac{dN_p}{dt} = -\frac{N_p}{\tau_p} - \gamma \frac{N_p}{\tau_R} - (N_S + 1) \frac{N_p}{\tau_R^{\text{cav}}} + \kappa_{\text{in}} P_p, \quad \text{(F1)}$$

$$\frac{dN_S}{dt} = -\frac{N_S}{\tau_S} + (N_S + 1) \frac{N_p}{\tau_R^{\text{cav}}}. \quad \text{(F2)}$$

Here, $\tau_S = Q_S/\omega_S$ and $\tau_p = Q_p/\omega_p$ are the Stokes and pump photon lifetimes, respectively. γ describes the Raman scattering into modes other than the cavity mode, and τ_R is a measure of the spontaneous Raman scattering lifetime in bulk. Stimulated (N_S) and spontaneous ($+1$) Raman scattering into the cavity mode is increased with respect to the bulk scattering rate via Purcell enhancement; the corresponding lifetime becomes τ_R^{cav}. The constant κ_{in} relates the injected pump photon number per time to the incident pump power P_p.

The spontaneous Raman scattering rate in bulk when the pump mode polarization is aligned along the $\langle 110 \rangle$ crystallographic axis can be calculated via [65]

$$\frac{1}{\tau_R} = \frac{2 g_R^B c^2 \hbar \omega_p}{3 n_p n_S V} M. \quad \text{(F3)}$$

Here, g_R^B denotes the bulk Raman gain and V the mode volume of a hypothetical, large cavity. M characterizes the total number of Raman modes into which the system can radiate for a cavity with mode volume V and frequency bandwidth $\delta\omega_R$ [102]:

$$M = \frac{V\omega_S^2 n_S^3}{2\pi c^3}\delta\omega_R. \tag{F4}$$

$\delta\omega_R$ describes the FWHM linewidth of the gain profile of the Raman scattering process. Hence,

$$\frac{1}{\tau_R} = \Gamma_R = \frac{\omega_S^2 n_S^2 g_R^B \hbar\omega_p \delta\omega_R}{3 n_p \pi c}. \tag{F5}$$

The cavity enhancement is given by a Lorentzian with amplitude F_P [44]. We approximate the Raman gain profile with a normalized Lorentzian [65]. We assume that the cavity is resonant with the Raman scattered light $\omega_S = \omega_R$:

$$\frac{1}{\tau_R^{cav}} = \frac{\omega_S^2 n_S^2 g_R^B \hbar\omega_p \delta\omega_R}{3 n_p \pi c} \int_0^\infty d\omega \times \frac{2}{\pi} \frac{\delta\omega_R}{4(\omega - \omega_S)^2 + \delta\omega_R^2}$$

$$\times F_P \frac{\delta\omega_S^2}{4(\omega - \omega_S)^2 + \delta\omega_S^2}. \tag{F6}$$

For $\omega_S \gg \delta\omega_S, \delta\omega_R$, the integrand is close to zero for $\omega = 0$, so the lower limit of the integral can be extended to negative infinity to obtain an analytical solution:

$$\frac{1}{\tau_R^{cav}} = \Gamma_R^{cav} = \frac{\omega_S^2 n_S^2 g_R^B \hbar\omega_p \delta\omega_R}{3 n_p \pi c} \frac{F_P \delta\omega_S}{\delta\omega_R + \delta\omega_S}. \tag{F7}$$

The Purcell enhancement of the system is given by

$$\frac{\Gamma_R^{cav}}{\Gamma_R} = F_P \frac{\delta\omega_S}{\delta\omega_R + \delta\omega_S}. \tag{F8}$$

This equation resembles the expression for Purcell enhancement of a two-level emitter in a regime in which the linewidth of the cavity and the coupled emitter are comparable [103–106]:

$$\frac{\Gamma_R^{cav}}{\Gamma_R} = \frac{3}{4\pi^2}\left(\frac{\lambda_S^{cav}}{n_S}\right)^3 \frac{1}{V_R} \frac{Q_S Q_R}{Q_S + Q_R}. \tag{F9}$$

The lasing threshold power P_{th} in the steady state can be calculated from

$$\Gamma_R^{cav} N_p (N_S + 1) = \frac{N_S}{\tau_S}. \tag{F10}$$

Using Eqs. (F1) and (F2),

$$\kappa_{in} P_{th} = \frac{N_S}{\tau_S}\left(\frac{1}{\Gamma_R^{cav}(N_S + 1)}\left(\frac{1}{\tau_p} + \frac{\gamma}{\tau_R}\right) + 1\right). \tag{F11}$$

Taking into account $N_S \gg 1$ and $\frac{1}{\tau_p} \gg \frac{1}{\tau_R}$,

$$\kappa_{in} P_{th} = \frac{1}{\tau_S \tau_p \Gamma_R^{cav}}, \tag{F12}$$

with $\kappa_{in} = \eta/(\hbar\omega_p)$:

$$\frac{\eta}{\hbar\omega_p} P_{th} = \frac{\omega_S \omega_p}{Q_S Q_p} \frac{n_S n_p V_R}{2\hbar\omega_p c^2 g_R^B} \frac{Q_S + Q_R}{Q_S}. \tag{F13}$$

We obtain the result for the lasing threshold:

$$P_{th} = \frac{1}{\eta}\frac{2 n_S n_p \pi^2}{\lambda_S^{cav}\lambda_p^{cav} g_R^B}\frac{V_R(Q_S + Q_R)}{Q_S^2 Q_p}. \tag{F14}$$

Table 1.   Summary of Experimental Parameters

t_a	1.80 μm	t_d	755 nm
λ_p^{cav}	634.57 nm	λ_S^{cav}	693.15 nm
n_p	2.4	n_S	2.4
τ_p^{-1}	$10.0 \times 10^9\,s^{-1}$	τ_R^{-1}	$2.38 \times 10^5\,s^{-1}$
Q_p	296900 ± 600	Q_S	6650 ± 50
Q_R	8960 ± 290	g_R^B	~40cm/GW [66]
η	0.45	V_R	108.3 μm³

We calculate the threshold power for the cavity used in the experiment. The parameters are listed in Table 1. The calculation yields $P_{th} = 189.3$ mW as stated in the main text.

APPENDIX G: FUTURE DIRECTIONS

We now turn to discuss some limiting factors and further possible improvements to this experiment. The double-resonance condition is satisfied for the combination of t_a and t_d for which both pump and Stokes modes are resonant simultaneously. With the current top mirror design (depth of curved mirror, $d = 1.65$ μm) and diamond thickness $t_d = 755$ nm, a relatively large air gap of $t_a = 4.18$ μm is required to meet this condition for the range of λ_{pump} available. The large air gap results in a large V_R, and consequently a large lasing threshold. Establishing the double-resonance condition for a shorter air gap will reduce V_R and consequently P_{th}.

We simulate the cavity for a wide range of t_a and t_d using $\lambda_p^{cav} = 634.57$ nm and $\lambda_S^{cav} = 693.15$ nm as before [Fig. 12(a)]. Reducing the diamond thickness to $t_d = 723$ nm satisfies the double-resonance condition for $t_a = 1.80$ μm. For this air gap, we calculate $V_R = 20.7$ μm³.

An additional benefit of reducing t_a becomes apparent on simulating the behavior of the Q-factor with increased cavity length [Fig. 12(b)]. The Q-factor and the cavity round-trip loss $\mathcal{L}_{cav}$ are linked via $Q = \frac{4\pi L_{cav}}{\lambda \mathcal{L}_{cav}}$, where $L_{cav} = t_a + L_0$. Here, the term L_0 describes the diamond thickness and the field penetration into the DBR mirror coatings [33,60]. For short cavity lengths, the Q-factor increases linearly with t_a. However, for large cavity lengths, the mode waist at the top mirror, w_I, becomes larger than the spherical extent of the mirror leading to beam clipping and a subsequent drop in the Q-factor [33,42,107]. For a spherical mirror with diameter D, the clipping losses are calculated according to $\mathcal{L}_{clip} = e^{-D^2/2w_I^2}$, where the beam waist w_I evolves according to [33]

$$w_I = \sqrt{\frac{\lambda R_{cav}}{\pi}} \times \left(\frac{R_{cav}}{(t_a + \frac{t_d}{n_d})} - 1\right)^{-\frac{1}{4}}. \tag{G1}$$

In Fig. 12(b), a drop in Q-factor is expected for $t_a \gtrsim 3.5$ μm, a consequence of clipping losses. Therefore, a shorter t_a will have the added benefit of preserving a high Q-factor. Here, the values of $R_{cav} = 11$ μm and $D = 6$ μm are extracted from a scanning confocal microscope (Keyence Corporation).

Using this model for $t_d = 723$ nm and $t_a = 1.80$ μm [dark blue circle in Fig. 12(a)], we find a theoretical $Q_p = 401,300$, $Q_S = 11,600$, $\eta = 0.81$, and consequently, $P_{th} = 6.32$ mW.

The diamond surface introduces scattering losses that should be taken into account. Surface scattering can be incorporated in the transfer-matrix simulations according to Refs. [33,108]. Motivated by typical roughness measurements reported by
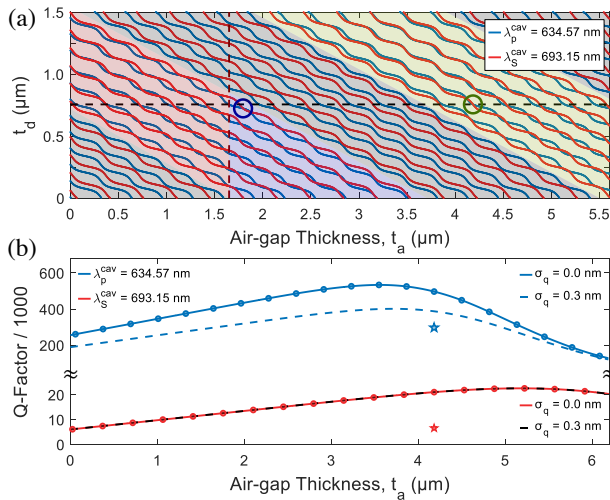
Fig. 12. (a) Simulated cavity mode structure for $\lambda_p^{cav} = 634.57$ nm (blue) and $\lambda_S^{cav} = 693.15$ nm (red) as a function of t_a and t_d. The double-resonance condition is satisfied for the pair of t_a and t_d where the two respective modes cross. The gray shaded areas indicate combinations of t_a and t_d for which the double-resonance condition cannot be satisfied for the particular combination of λ_p^{cav} and λ_S^{cav}. The green circle high-lights the combination $t_a = 4.18$ μm and $t_d = 755$ nm (horizontal black dashed line) used in this experiment. The vertical burgundy dashed line represents the depth of the curved mirror, $d = 1.65$ μm, setting the lower limit on the accessible t_a in the current cavity geometry. The red shaded area represents possible combinations of t_a and t_d that would be accessible with a shallower curved mirror. The blue and green shaded regions show combinations of t_a and t_d where the double-resonance condition is satisfied for adjacent, i.e., $\Delta q_{eff} = 1$, and second-adjacent, i.e., $\Delta q_{eff} = 2$, cavity modes, respectively. Reducing the diamond thick-ness by 32 nm to $t_d = 723$ nm satisfies the double-resonance condition for $t_a = 1.80$ μm (blue circle). For details, see text. (b) Simulated dependence of the Q-factor with air-gap thickness for fixed $\lambda_p^{cav} = 634.57$ nm (blue) and $\lambda_S^{cav} = 693.15$ nm (red). The solid lines represent the Q-factor in the absence of any losses, while the dashed lines represent the Q-factor in the presence of surface scattering with surface roughness $\sigma_q = 0.3$ nm. The drop in Q-factor at large air-gap thicknesses is attributed to clipping losses at the top mirror. The experimentally measured Q-factors are indicated by the stars. The Q-factor at λ_p agrees well with the simulations including surface scattering. At λ_S, the measured Q-factor is substantially lower than the simulated Q-factor. This arises because λ_S is close to the edge of the stopband and therefore depends sensitively on the exact layer thicknesses in the DBRs, which are not known precisely.

Refs. [33,55], including a scattering layer with surface rough-ness $\sigma_q = 0.3$ nm reduces the Q-factors to $Q_p^{scat} = 258,070$ and $Q_S^{scat} = 11,540$. The additional loss channel results in $\eta^{scat} = 0.60$. The reduction in the Q-factor increases the lasing threshold to $P_{th}^{scat} = 13.4$ mW. Finally, increasing the thickness of the diamond membrane provides a way to reduce further the lasing threshold on account of the larger Q-factor offered by the longer effective cavity length. Applying the same method as in Fig. 12(a), we find that the double-resonance condition is established for $t_d = 3.37$ μm and $t_a = 1.73$ μm. Using these values and simulating a loss-less cavity yields $P_{th} = 1.00$ mW. Including surface scattering ($\sigma_q = 0.3$ nm) increases the threshold to $P_{th} = 2.37$ mW.

REFERENCES

1. K. J. Vahala, "Optical microcavities," Nature **424**, 839–846 (2003).
2. D. Najer, I. Söllner, P. Sekatski, V. Dolique, M. C. Löbl, D. Riedel, R. Schott, S. Starosielec, S. R. Valentin, A. D. Wieck, N. Sangouard, A. Ludwig, and R. J. Warburton, "A gated quantum dot strongly coupled to an optical microcavity," Nature **575**, 622–627 (2019).
3. A. Matsko and V. Ilchenko, "Optical resonators with whispering-gallery modes-part I: basics," IEEE J. Sel. Top. Quantum Electron. **12**, 3–14 (2006).
4. V. Ilchenko and A. Matsko, "Optical resonators with whispering-gallery modes-part II: applications," IEEE J. Sel. Top. Quantum Electron. **12**, 15–32 (2006).
5. D. V. Strekalov, C. Marquardt, A. B. Matsko, H. G. L. Schwefel, and G. Leuchs, "Nonlinear and quantum optics with whispering gallery resonators," J. Opt. **18**, 123002 (2016).
6. G. Lin, A. Coillet, and Y. K. Chembo, "Nonlinear photonics with high-Q whispering-gallery-mode resonators," Adv. Opt. Photon. **9**, 828–890 (2017).
7. B. J. M. Hausmann, I. Bulu, V. Venkataraman, P. Deotare, and M. Lončar, "Diamond nonlinear photonics," Nat. Photonics **8**, 369–374 (2014).
8. P. Latawiec, V. Venkataraman, M. J. Burek, B. J. M. Hausmann, I. Bulu, and M. Lončar, "On-chip diamond Raman laser," Optica **2**, 924–928 (2015).
9. P. Latawiec, V. Venkataraman, A. Shams-Ansari, M. Markham, and M. Lončar, "Integrated diamond Raman laser pumped in the near-visible," Opt. Lett. **43**, 318–321 (2018).
10. P. K. Shandilya, S. Flågan, N. C. Carvalho, E. Zohari, V. K. Kavatamane, J. E. Losby, and P. E. Barclay, "Diamond integrated quantum nanopho-tonics: spins, photons, and phonons," J. Lightwave Technol. (2022), Early Access.
11. S. M. Spillane, T. J. Kippenberg, and K. J. Vahala, "Ultralow-threshold Raman laser using a spherical dielectric microcavity," Nature **415**, 621–623 (2002).
12. T. J. Kippenberg, S. M. Spillane, D. K. Armani, and K. J. Vahala, "Ultralow-threshold microcavity Raman laser on a microelectronic chip," Opt. Lett. **29**, 1224–1226 (2004).
13. D. M. Lukin, C. Dory, M. A. Guidry, K. Y. Yang, S. D. Mishra, R. Trivedi, M. Radulaski, S. Sun, D. Vercruysse, G. H. Ahn, and J. Vučković, "4H-silicon-carbide-on-insulator for integrated quantum and nonlinear pho-tonics," Nat. Photonics **14**, 330–334 (2020).
14. M. A. Guidry, K. Y. Yang, D. M. Lukin, A. Markosyan, J. Yang, M. M. Fejer, and J. Vučković, "Optical parametric oscillation in silicon carbide nanophotonics," Optica **7**, 1139–1142 (2020).
15. M. A. Guidry, D. M. Lukin, K. Y. Yang, R. Trivedi, and J. Vučković, "Quantum optics of soliton microcombs," Nat. Photonics **16**, 52–58 (2022).
16. Y. Liu, M. Davanço, V. Aksyuk, and K. Srinivasan, "Electromagnetically induced transparency and wideband wavelength conversion in silicon nitride microdisk optomechanical resonators," Phys. Rev. Lett. **110**, 223603 (2013).
17. X. Ji, F. A. S. Barbosa, S. P. Roberts, A. Dutt, J. Cardenas, Y. Okawachi, A. Bryant, A. L. Gaeta, and M. Lipson, "Ultra-low-loss on-chip res-onators with sub-milliwatt parametric oscillation threshold," Optica **4**, 619–624 (2017).
18. X. Lu, Q. Li, D. A. Westly, G. Moille, A. Singh, V. Anant, and K. Srinivasan, "Chip-integrated visible–telecom entangled photon pair source for quantum communication," Nat. Phys. **15**, 373–381 (2019).
19. R. Wu, J. Zhang, N. Yao, W. Fang, L. Qiao, Z. Chai, J. Lin, and Y. Cheng, "Lithium niobate micro-disk resonators of quality factors above 10^7," Opt. Lett. **43**, 4116–4119 (2018).

20. D. Zhu, L. Shao, M. Yu, R. Cheng, B. Desiatov, C. J. Xin, Y. Hu, J. Holzgrafe, S. Ghosh, A. Shams-Ansari, E. Puma, N. Sinclair, C. Reimer, M. Zhang, and M. Lončar, "Integrated photonics on thin-film lithium niobate," Adv. Opt. Photon. **13**, 242–352 (2021).

21. D. P. Lake, M. Mitchell, H. Jayakumar, L. F. dos Santos, D. Curic, and P. E. Barclay, "Efficient telecom to visible wavelength conversion in doubly resonant gallium phosphide microdisks," Appl. Phys. Lett. **108**, 031109 (2016).

22. A. D. Logan, M. Gould, E. R. Schmidgall, K. Hestroffer, Z. Lin, W. Jin, A. Majumdar, F. Hatami, A. W. Rodriguez, and K.-M. C. Fu, "W second harmonic conversion efficiency in 14 m-diameter gallium phosphide-on-oxide resonators," Opt. Express **26**, 33687–33699 (2018).

23. D. J. Wilson, K. Schneider, S. Hönl, M. Anderson, Y. Baumgartner, L. Czornomaz, T. J. Kippenberg, and P. Seidler, "Integrated gallium phosphide nonlinear photonics," Nat. Photonics **14**, 57–62 (2020).

24. B. McLaughlin, D. P. Lake, M. Mitchell, and P. E. Barclay, "Nonlinear optics in gallium phosphide cavities: simultaneous second and third harmonic generation," J. Opt. Soc. Am. B **39**, 1853–1860 (2022).

25. A. Das, D. J. Lee, P. K. Shandilya, S. Kim, G. Kang, D. P. Lake, B. Behera, D. Sukachev, I. Aharonovich, J.-H. Lee, J. Park, and P. E. Barclay, "Demonstration of hybrid high- Q hexagonal boron nitride microresonators," ACS Photon. **8**, 3027–3033 (2021).

26. X. Shen, H. Choi, D. Chen, W. Zhao, and A. M. Armani, "Raman laser from an optical resonator with a grafted single-molecule monolayer," Nat. Photonics **14**, 95–101 (2020).

27. I. Roland, M. Gromovyi, Y. Zeng, M. El Kurdi, S. Sauvage, C. Brimont, T. Guillet, B. Gayral, F. Semond, J. Y. Duboz, M. de Micheli, X. Checoury, and P. Boucaud, "Phase-matched second harmonic generation with on-chip GaN-on-Si microdisks," Sci. Rep. **6**, 34191 (2016).

28. X. Lu, S. Rogers, W. C. Jiang, and Q. Lin, "Selective engineering of cavity resonance for frequency matching in optical parametric processes," Appl. Phys. Lett. **105**, 151104 (2014).

29. X. Lu, A. Rao, G. Moille, D. A. Westly, and K. Srinivasan, "Universal frequency engineering tool for microcavity nonlinear optics: multiple selective mode splitting of whispering-gallery resonances," Photon. Res. **8**, 1676–1686 (2020).

30. G. Lin and N. Yu, "Continuous tuning of double resonance-enhanced second harmonic generation in a dispersive dielectric resonator," Opt. Express **22**, 557–562 (2014).

31. M. Brekenfeld, D. Niemietz, J. D. Christesen, and G. Rempe, "A quantum network node with crossed optical fibre cavities," Nat. Phys. **16**, 647–651 (2020).

32. M. Sumetsky, "Mahaux-Weidenmüller approach to cavity quantum electrodynamics and complete resonant down-conversion of the single-photon frequency," Phys. Rev. A **100**, 013801 (2019).

33. S. Flågan, D. Riedel, A. Javadi, T. Jakubczyk, P. Maletinsky, and R. J. Warburton, "A diamond-confined open microcavity featuring a high quality-factor and a small mode-volume," J. Appl. Phys. **131**, 113102 (2022).

34. D. Wang, H. Kelkar, D. Martin-Cano, D. Rattenbacher, A. Shkarin, T. Utikal, S. Götzinger, and V. Sandoghdar, "Turning a molecule into a coherent two-level quantum system," Nat. Phys. **15**, 483–489 (2019).

35. E. Janitz, M. Ruf, M. Dimock, A. Bourassa, J. Sankey, and L. Childress, "Fabry-Perot microcavity for diamond-based photonics," Phys. Rev. A **92**, 043844 (2015).

36. A. B. Matsko, A. A. Savchenkov, R. J. Letargat, V. S. Ilchenko, and L. Maleki, "On cavity modification of stimulated Raman scattering," J. Opt. B **5**, 272–278 (2003).

37. R. P. Mildren and J. R. Rabeau, *Optical Engineering of Diamond* (Wiley, 2013).

38. A. M. Zaitsev, *Optical Properties of Diamond* (Springer, 2010).

39. M. D. Anderson, S. Tarrago Velez, K. Seibold, H. Flayac, V. Savona, N. Sangouard, and C. Galland, "Two-color pump-probe measurement of photonic quantum correlations mediated by a single phonon," Phys. Rev. Lett. **120**, 233601 (2018).

40. K. C. Lee, B. J. Sussman, M. R. Sprague, P. Michelberger, K. F. Reim, J. Nunn, N. K. Langford, P. J. Bustard, D. Jaksch, and I. A. Walmsley, "Macroscopic non-classical states and terahertz quantum processing in room-temperature diamond," Nat. Photonics **6**, 41–44 (2012).

41. D. Riedel, S. Flågan, P. Maletinsky, and R. J. Warburton, "Cavity-enhanced Raman scattering for in situ alignment and characterization of solid-state microcavities," Phys. Rev. Appl. **13**, 014036 (2020).

42. D. Hunger, T. Steinmetz, Y. Colombe, C. Deutsch, T. W. Hänsch, and J. Reichel, "A fiber Fabry–Perot cavity with high finesse," New J. Phys. **12**, 065038 (2010).

43. A. Muller, E. B. Flagg, J. R. Lawall, and G. S. Solomon, "Ultrahigh-finesse, low-mode-volume Fabry–Perot microcavity," Opt. Lett. **35**, 2293–2295 (2010).

44. R. J. Barbour, P. A. Dalgarno, A. Curran, K. M. Nowak, H. J. Baker, D. R. Hall, N. G. Stoltz, P. M. Petroff, and R. J. Warburton, "A tunable microcavity," J. Appl. Phys. **110**, 053107 (2011).

45. L. Greuter, S. Starosielec, D. Najer, A. Ludwig, L. Duempelmann, D. Rohner, and R. J. Warburton, "A small mode volume tunable microcavity: development and characterization," Appl. Phys. Lett. **105**, 121105 (2014).

46. T. Hümmer, J. Noe, M. S. Hofmann, T. W. Hänsch, A. Högele, and D. Hunger, "Cavity-enhanced Raman microscopy of individual carbon nanotubes," Nat. Commun. **7**, 12155 (2016).

47. D. Hunger, C. Deutsch, R. J. Barbour, R. J. Warburton, and J. Reichel, "Laser micro-fabrication of concave, low-roughness features in silica," AIP Adv. **2**, 012119 (2012).

48. N. Tomm, A. Javadi, N. O. Antoniadis, D. Najer, M. C. Löbl, A. R. Korsch, R. Schott, S. R. Valentin, A. D. Wieck, A. Ludwig, and R. J. Warburton, "A bright and fast source of coherent single photons," Nat. Nanotechnol. **16**, 399–403 (2021).

49. D. Riedel, D. Rohner, M. Ganzhorn, T. Kaldewey, P. Appel, E. Neu, R. J. Warburton, and P. Maletinsky, "Low-loss broadband antenna for efficient photon collection from a coherent spin in diamond," Phys. Rev. Appl. **2**, 064011 (2014).

50. D. Riedel, I. Söllner, B. J. Shields, S. Starosielec, P. Appel, E. Neu, P. Maletinsky, and R. J. Warburton, "Deterministic enhancement of coherent photon generation from a nitrogen-vacancy center in ultrapure diamond," Phys. Rev. X **7**, 031040 (2017).

51. S. Häußler, J. Benedikter, K. Bray, B. Regan, A. Dietrich, J. Twamley, I. Aharonovich, D. Hunger, and A. Kubanek, "Diamond photonics platform based on silicon vacancy centers in a single-crystal diamond membrane and a fiber cavity," Phys. Rev. B **99**, 165310 (2019).

52. S. Bogdanović, S. B. van Dam, C. Bonato, L. C. Coenen, A.-M. J. Zwerver, B. Hensen, M. S. Z. Liddy, T. Fink, A. Reiserer, M. Lončar, and R. Hanson, "Design and low-temperature characterization of a tunable microcavity for diamond-based quantum networks," Appl. Phys. Lett. **110**, 171103 (2017).

53. R. Høy Jensen, E. Janitz, Y. Fontana, Y. He, O. Gobron, I. P. Radko, M. Bhaskar, R. Evans, C. D. Rodríguez Rosenblueth, L. Childress, A. Huck, and U. Lund Andersen, "Cavity-enhanced photon emission from a single germanium-vacancy center in a diamond membrane," Phys. Rev. Appl. **13**, 064016 (2020).

54. M. Ruf, M. Weaver, S. van Dam, and R. Hanson, "Resonant excitation and purcell enhancement of coherent nitrogen-vacancy centers coupled to a Fabry-Perot microcavity," Phys. Rev. Appl. **15**, 024049 (2021).

55. P. Appel, E. Neu, M. Ganzhorn, A. Barfuss, M. Batzer, M. Gratz, A. Tschöpe, and P. Maletinsky, "Fabrication of all diamond scanning probes for nanoscale magnetometry," Rev. Sci. Instrum. **87**, 063703 (2016).

56. M. Challier, S. Sonusen, A. Barfuss, D. Rohner, D. Riedel, J. Koelbl, M. Ganzhorn, P. Appel, P. Maletinsky, and E. Neu, "Advanced fabrication of single-crystal diamond membranes for quantum technologies," Micromachines **9**, 148 (2018).

57. J. Heupel, M. Pallmann, J. Körber, R. Merz, M. Kopnarski, R. Stöhr, J. P. Reithmaier, D. Hunger, and C. Popov, "Fabrication and characterization of single-crystal diamond membranes for quantum photonics with tunable microcavities," Micromachines **11**, 1080 (2020).

58. B. Petrak, N. Djeu, and A. Muller, "Purcell-enhanced Raman scattering from atmospheric gases in a high-finesse microcavity," Phys. Rev. A **89**, 023811 (2014).

59. H. Kelkar, D. Wang, D. Martín-Cano, B. Hoffmann, S. Christiansen, S. Götzinger, and V. Sandoghdar, "Sensing nanoparticles with a cantilever-based scannable optical cavity of low finesse and sub-volume," Phys. Rev. Appl. **4**, 054010 (2015).

60. C. Koks and M. P. van Exter, "Microcavity resonance condition, quality factor, and mode volume are determined by different penetration depths," Opt. Express **29**, 6879–6889 (2021).

61. A. C. Ferrari and J. Robertson, "Interpretation of Raman spectra of disordered and amorphous carbon," Phys. Rev. B **61**, 14095–14107 (2000).

62. S. Prawer and R. J. Nemanich, "Raman spectroscopy of diamond and doped diamond," Philos. Trans. R. Soc. Lond. A: Math. Phys. Eng. Sci. **362**, 2537–2565 (2004).

63. E. Janitz, M. K. Bhaskar, and L. Childress, "Cavity quantum electrodynamics with color centers in diamond," Optica **7**, 1232–1252 (2020).

64. X. Yang and C. W. Wong, "Coupled-mode theory for stimulated Raman scattering in high- silicon photonic band gap defect cavity lasers," Opt. Express **15**, 4763–4780 (2007).

65. X. Checoury, Z. Han, M. El Kurdi, and P. Boucaud, "Deterministic measurement of the Purcell factor in microcavities through Raman emission," Phys. Rev. A **81**, 033832 (2010).

66. V. G. Savitski, S. Reilly, and A. J. Kemp, "Steady-state Raman gain in diamond as a function of pump wavelength," IEEE J. Quantum Electron. **49**, 218–223 (2013).

67. W. Nagourney, *Quantum Electronics for Atomic Physics and Telecommunication*, 2nd ed. (Oxford University, 2014).

68. J. Gallego, S. Ghosh, S. K. Alavi, W. Alt, M. Martinez-Dorantes, D. Meschede, and L. Ratschbacher, "High-finesse fiber Fabry–Perot cavities: stabilization and mode matching analysis," Appl. Phys. B **122**, 47 (2016).

69. D. J. Spence, E. Granados, and R. P. Mildren, "Mode-locked picosecond diamond Raman laser," Opt. Lett. **35**, 556–558 (2010).

70. X. Yang, O. Kitzler, D. J. Spence, Z. Bai, Y. Feng, and R. P. Mildren, "Diamond sodium guide star laser," Opt. Lett. **45**, 1898–1901 (2020).

71. O. Kitzler, J. Lin, H. M. Pask, R. P. Mildren, S. C. Webster, N. Hempler, G. P. A. Malcolm, and D. J. Spence, "Single-longitudinal-mode ring diamond Raman laser," Opt. Lett. **42**, 1229–1232 (2017).

72. A. D. Greentree and S. Prawer, "A little diamond goes a long way," Nat. Photonics **4**, 202–203 (2010).

73. R. P. Mildren, J. E. Butler, and J. R. Rabeau, "CVD-diamond external cavity Raman laser at 573 nm," Opt. Express **16**, 18950–18955 (2008).

74. R. P. Mildren and A. Sabella, "Highly efficient diamond Raman laser," Opt. Lett. **34**, 2811–2813 (2009).

75. Q. Sheng, R. Li, A. J. Lee, D. J. Spence, and H. M. Pask, "A single-frequency intracavity Raman laser," Opt. Express **27**, 8540–8553 (2019).

76. E. Granados, D. J. Spence, and R. P. Mildren, "Deep ultraviolet diamond Raman laser," Opt. Express **19**, 10857–10863 (2011).

77. K. Chrysalidis, V. N. Fedosseev, B. A. Marsh, R. P. Mildren, D. J. Spence, K. D. A. Wendt, S. G. Wilkins, and E. Granados, "Continuously tunable diamond Raman laser for resonance laser ionization," Opt. Lett. **44**, 3924–3927 (2019).

78. W. Lubeigt, G. M. Bonner, J. E. Hastie, M. D. Dawson, D. Burns, and A. J. Kemp, "Continuous-wave diamond Raman laser," Opt. Lett. **35**, 2994–2996 (2010).

79. D. C. Parrotta, A. J. Kemp, M. D. Dawson, and J. E. Hastie, "Multiwatt, continuous-wave, tunable diamond Raman laser with intracavity frequency-doubling to the visible region," IEEE J. Sel. Top. Quantum Electron. **19**, 1400108 (2013).

80. O. Kitzler, A. McKay, and R. P. Mildren, "Continuous-wave wavelength conversion for high-power applications using an external cavity diamond Raman laser," Opt. Lett. **37**, 2790–2792 (2012).

81. A. Sabella, J. A. Piper, and R. P. Mildren, "1240 nm diamond Raman laser operating near the quantum limit," Opt. Lett. **35**, 3874–3876 (2010).

82. A. Sabella, J. A. Piper, and R. P. Mildren, "Efficient conversion of a 1064 m Nd:YAG laser to the eye-safe region using a diamond Raman laser," Opt. Express **19**, 23554–23560 (2011).

83. J.-P. M. Feve, K. E. Shortoff, M. J. Bohn, and J. K. Brasseur, "High average power diamond Raman laser," Opt. Express **19**, 913–922 (2011).

84. R. J. Williams, O. Kitzler, A. McKay, and R. P. Mildren, "Investigating diamond Raman lasers at the 100 W level using quasi-continuous-wave pumping," Opt. Lett. **39**, 4152–4155 (2014).

85. S. Antipov, A. Sabella, R. J. Williams, O. Kitzler, D. J. Spence, and R. P. Mildren, "12 kW quasi-steady-state diamond Raman laser pumped by an M^2=15 beam," Opt. Lett. **44**, 2506–2509 (2019).

86. R. Casula, J.-P. Penttinen, A. J. Kemp, M. Guina, and J. E. Hastie, "14 μm continuous-wave diamond Raman laser," Opt. Express **25**, 31377–31383 (2017).

87. S. G. Pavlov, N. Deßmann, B. Redlich, A. F. G. van der Meer, N. V. Abrosimov, H. Riemann, R. K. Zhukavin, V. N. Shastin, and H.-W. Hübers, "Competing inversion-based lasing and Raman lasing in doped silicon," Phys. Rev. X **8**, 041003 (2018).

88. H. Rong, R. Jones, A. Liu, O. Cohen, D. Hak, A. Fang, and M. Paniccia, "A continuous-wave Raman silicon laser," Nature **433**, 725–728 (2005).

89. H. Rong, A. Liu, R. Jones, O. Cohen, D. Hak, R. Nicolaescu, A. Fang, and M. Paniccia, "An all-silicon Raman laser," Nature **433**, 292–294 (2005).

90. H. Rong, S. Xu, O. Cohen, O. Raday, M. Lee, V. Sih, and M. Paniccia, "A cascaded silicon Raman laser," Nat. Photonics **2**, 170–174 (2008).

91. Y. Takahashi, Y. Inui, M. Chihara, T. Asano, R. Terawaki, and S. Noda, "A micrometre-scale Raman silicon laser with a microwatt threshold," Nature **498**, 470–474 (2013).

92. M. Yu, Y. Okawachi, R. Cheng, C. Wang, M. Zhang, A. L. Gaeta, and M. Lončar, "Raman lasing and soliton mode-locking in lithium niobate microresonators," Light Sci. Appl. **9**, 9 (2020).

93. C. Wang, Z. Fang, A. Yi, B. Yang, Z. Wang, L. Zhou, C. Shen, Y. Zhu, Y. Zhou, R. Bao, Z. Li, Y. Chen, K. Huang, J. Zhang, Y. Cheng, and X. Ou, "High-Q microresonators on 4H-silicon-carbide-on-insulator platform for nonlinear photonics," Light Sci. Appl. **10**, 139 (2021).

94. X. Liu, C. Sun, B. Xiong, L. Wang, J. Wang, Y. Han, Z. Hao, H. Li, Y. Luo, J. Yan, T. Wei, Y. Zhang, and J. Wang, "Integrated continuous-wave aluminum nitride Raman laser," Optica **4**, 893–896 (2017).

95. R. J. Williams, O. Kitzler, Z. Bai, S. Sarang, H. Jasbeer, A. McKay, S. Antipov, A. Sabella, O. Lux, D. J. Spence, and R. P. Mildren, "High power diamond Raman lasers," IEEE J. Sel. Top. Quantum Electron. **24**, 1602214 (2018).

96. D. M. Lukin, M. A. Guidry, and J. Vučković, "Integrated quantum photonics with silicon carbide: challenges and prospects," PRX Quantum **1**, 020102 (2020).

97. T. P. McKenna, H. S. Stokowski, V. Ansari, J. Mishra, M. Jankowski, C. J. Sarabalis, J. F. Herrmann, C. Langrock, M. M. Fejer, and A. H. Safavi-Naeini, "Ultra-low-power second-order nonlinear optics on a chip," Nat. Commun. **13**, 4532 (2022).

98. D. Najer, N. Tomm, A. Javadi, A. R. Korsch, B. Petrak, D. Riedel, V. Dolique, S. R. Valentin, R. Schott, A. D. Wieck, A. Ludwig, and R. J. Warburton, "Suppression of surface-related loss in a gated semiconductor microcavity," Phys. Rev. Appl. **15**, 044004 (2021).

99. P. Maletinsky, S. Hong, M. S. Grinolds, B. Hausmann, M. D. Lukin, R. L. Walsworth, M. Loncar, and A. Yacoby, "A robust scanning diamond sensor for nanoscale imaging with single nitrogen-vacancy centres," Nat. Nanotechnol. **7**, 320–324 (2012).

100. X. Checoury, Z. Han, and P. Boucaud, "Stimulated Raman scattering in silicon photonic crystal waveguides under continuous excitation," Phys. Rev. B **82**, 041308 (2010).

101. S. B. van Dam, M. Ruf, and R. Hanson, "Optimal design of diamond-air microcavities for quantum networks using an analytical approach," New J. Phys. **20**, 115004 (2018).

102. R. W. Boyd, *Nonlinear Optics* (Academic, 1992).

103. H. Kaupp, T. Hümmer, M. Mader, B. Schlederer, J. Benedikter, P. Haeusser, H.-C. Chang, H. Fedder, T. W. Hänsch, and D. Hunger, "Purcell-enhanced single-photon emission from nitrogen-vacancy centers coupled to a tunable microcavity," Phys. Rev. Appl. **6**, 054010 (2016).

104. B. Romeira and A. Fiore, "Purcell effect in the stimulated and spontaneous emission rates of nanoscale semiconductor lasers," IEEE J. Quantum Electron. **54**, 2000412 (2018).

105. A. Auffèves, D. Gerace, J.-M. Gérard, M. F. Santos, L. C. Andreani, and J.-P. Poizat, "Controlling the dynamics of a coupled atom-cavity system by pure dephasing," Phys. Rev. B **81**, 245419 (2010).

106. A. Meldrum, P. Bianucci, and F. Marsiglio, "Modification of ensemble emission rates and luminescence spectra for inhomogeneously broadened distributions of quantum dots coupled to optical microcavities," Opt. Express **18**, 10230–10246 (2010).

107. J. Benedikter, T. Hümmer, M. Mader, B. Schlederer, J. Reichel, T. W. Hänsch, and D. Hunger, "Transverse-mode coupling and diffraction loss in tunable Fabry–Pérot microcavities," New J. Phys. **17**, 053051 (2015).

108. C. K. Carniglia and D. G. Jensen, "Single-layer model for surface roughness," Appl. Opt. **41**, 3167–3171 (2002).